nanomaterials

MDPI

Article

Thermoelectric Properties of $NiCl_3$ Monolayer: A First-Principles-Based Transport Study

Jing Liu, Xiaorui Chen, Yuhong Huang, Hongkuan Yuan and Hong Chen *

School of Physical Science and Technology, Southwest University, Chongqing 400715, China; jingliu2112@163.com (J.L.); chenxr0909@163.com (X.C.); huangyh211@163.com (Y.H.); yhk10@swu.edu.cn (H.Y.)
* Correspondence: chenh@swu.edu.cn

Received: 13 January 2020; Accepted: 20 February 2020; Published: 27 February 2020

Abstract: By employing the first-principles-based transport theory, we investigate the thermoelectric performance based on the structural and electronic properties of $NiCl_3$ monolayer. The $NiCl_3$ monolayer is confirmed to be a stable Dirac spin gapless semiconductor with the linear energy dispersion having almost massless carrier, high carrier mobility and fully spin-polarization. Further, $NiCl_3$ monolayer processes the optimum power factor of 4.97 mWm^{-1} K^{-2}, the lattice thermal conductivity of 1.89 Wm^{-1} K^{-1}, and the dimensionless figure of merit of 0.44 at room temperature under reasonable carrier concentration, indicating that $NiCl_3$ monolayer may be a potential matrix for promising thermoelectrics.

Keywords: two-dimensional transition metal halide; spin-gapless semiconductor; thermoelectrics; power factor; lattice thermal conductivity; figure of merit

1. Introduction

Recently, two-dimensional (2D) transition metal trihalides have stimulated a large number of interest due to the low dimensional magnetism. These compounds in their bulk phase are known to exist in the form of layered materials bonded to one another through weak van der Waals interactions [1]. Generally, all of the layered compounds have been reported to adopt either the monoclinic $AlCl_3$-type structure or the rhombohedral BiI_3-type structure. They can be easily exfoliated into atomically thin 2D materials from their bulk phases due to the weak interlayer van der Waals interactions. Several transition metal halide monolayers have been successfully prepared experimentally and their magnetism have been reported [2–4]. Some transition metal halide monolayers have been theoretically predicted to have ferromagnetic or anti-ferromagnetic ground states [5–17]. Among them, Ni-bases trihalides is theoretically predicted to be Dirac spin-gapless semiconductor with the Curie temperature above room temperatures [10,16,18]. However, relevant works about lattice thermal conductivity and thermoelectric (TE) properties of these monolayers are still lacking to date.

Generally, the thermally-driven electrical performance of TE materials is measured by the power factor $PF = S^2\sigma$, in which S and σ are respectively Seebeck coefficient and electrical conductivity, while a high heat-to-electricity conversion efficiency is scaled by the dimensionless figure of merit $zT = S^2\sigma T/(\kappa_e + \kappa_l)$ [19,20], where T is the absolute temperature, κ_e and κ_l are electronic and lattice thermal conductivity, respectively. Obviously, the prerequisite for thermoelectrics to efficiently convert unavoidable waste heat is to search for optimum zT materials to possess a maximum PF and simultaneously a minimum κ. Unfortunately, S and σ unusually interweave and behave in an opposite trend [21], and σ is proportional to κ_e as governed by Wiedemann-Franz's law. Thus, the improvement of thermoelectric devices strongly depends on the optimization of electronic and thermal transport properties of TE materials. Fortunately, the 2D materials could alleviate the coupling between S and σ due to the quantum confinement effects [22,23], consequently enhancing thermoelectric performance [24–26].

Typically, the 2D $NiCl_3$ monolayer is predicted theoretically to be robust ferromagnetic Dirac spin-gapless semiconductor and process the Curie temperature above the room temperature [10,16]. Its Fermi velocity (v_F) is 4.00×10^5 m/s, approaching half that of natural graphene (8.50×10^5 m/s). The energetically, dynamically and mechanically stability of the material was further confirmed by its Young's modulus calculation and *ab initio* molecular dynamics (AIMD) simulations. The zero gap between Dirac cones will be opened in $NiCl_3$ monolayer with consideration of spin-orbital coupling (SOC) [10]. Thus, $NiCl_3$ monolayer can also be transformed to be a Chern insulator. The unique band structure of $NiCl_3$ monolayer enable it to be promising for developing efficient thermoelectrics. In this work, we evaluate the lattice thermal conductivity and thermoelectric properties of $NiCl_3$ monolayer by using first-principles in combination with Boltzmann transport theory.

2. Computational Process

Firstly, we determine the stable configuration and the corresponding energy band structure of $NiCl_3$ monolayer by employing the density functional theory (DFT) as implemented by the Vienna Ab-initio simulation package (VASP) [27–29] with projector-augmented wave (PAW) method [30]. The Perdew-Burke-Ernzerhof (PBE) [31] manner with generalized gradient approximation (GGA) is selected as the exchange-correlation functional. After a strict convergence test, a plane-wave kinetic energy cutoff of 500 eV is adopted and $15 \times 15 \times 1$ k-mesh is chosen as the Monkhorst-Pack uniform k-point sampling [32] in the Brillouin zone. The structure is fully relaxed until the energy difference between two successive ionic relaxation steps is less than 10^{-6} eV and the forces on each atom are less than 0.01 eV/Å. Perpendicular to the monolayers, a vacuum of 15 Å is applied to prevent the spurious interactions between the adjacent $NiCl_3$ monolayers among replica images.

Secondly, having the information of the band structure, we estimate the electronic transport properties of the $NiCl_3$ monolayer, including S, σ, and κ_e by applying the semi-classical Boltzmann transport theory within the relaxation time approximation as implemented in the BoltzTrap code [33]. Since the σ and κ_e are proportional to the relaxation time (τ), it is of great importance to accurately obtain τ. As a matter of fact, τ in materials is a function of temperature and carrier concentration. So far experimental measurement is the only effective route to obtain τ [34,35]. Many earlier theoretical calculations on σ and κ_e were performed by adopting a constant relaxation time approximation [36–38], which is generally overestimated [39–41]. In this work, the relaxation time is evaluated by adopting the deformation potential (DP) theory [42], which was widely used to calculate the relaxation time for two-dimensional systems [43–47].

Finally, the lattice thermal conductivity (κ_l) can be obtained by solving the phonon Boltzmann transformation related to the harmonic and anharmonic interatomic force constants as performed by the ShengBTE code [48–50], which takes harmonic second-order interatomic force constants (2nd IFCS) and anharmonic thirdorder IFCs (3rd IFCS) as inputs. The second-order IFCs of monolayer $NiCl_3$ were computed using finite-difference method by the Phonopy code [51] using a $4 \times 4 \times 4$ supercell with $5 \times 5 \times 1$ k-point sampling. The anharmonic 3rd IFCS are obtained by Thirdorder code using a $4 \times 4 \times 4$ supercell and Γ-point only calculations.

3. Results and Discussion

3.1. Crystal and Electronic Structures

Two-dimensional $NiCl_3$ layer has a hexagonal crystal structure with the No. 162 space group. Ni atoms are arranged in a two-dimensional hexagonal honeycomb shape. The six nearest Cl atoms around the Ni atom form an octahedron. Each Ni atom is the center of the octahedron, and Cl atoms are located at the six vertices of the octahedron. The obtained stable structure of 2D $NiCl_3$ with the lowest energy by fully relaxing the atomic position is shown in Figure 1. After considering the DFT-D3 dispersion correction method, the Ni-Cl bond length is 2.30 Å and a lattice parameter is 5.96 Å, which is consistent with the previous theoretical work [10]. The calculated value of magnetic moment per Ni

atom is 0.94 μ_B. The total magnetic moment is 2 μ_B per unit cell. The ferromagnetic ground state can be identified by non-zero total magnetic moment per unit cell, which originates primarily from Ni atom. Based on calculated value of magnetic moment, Ni^{3+} is found to exist in low spin state (1 μ_B) [16] due to high crystal field splitting.

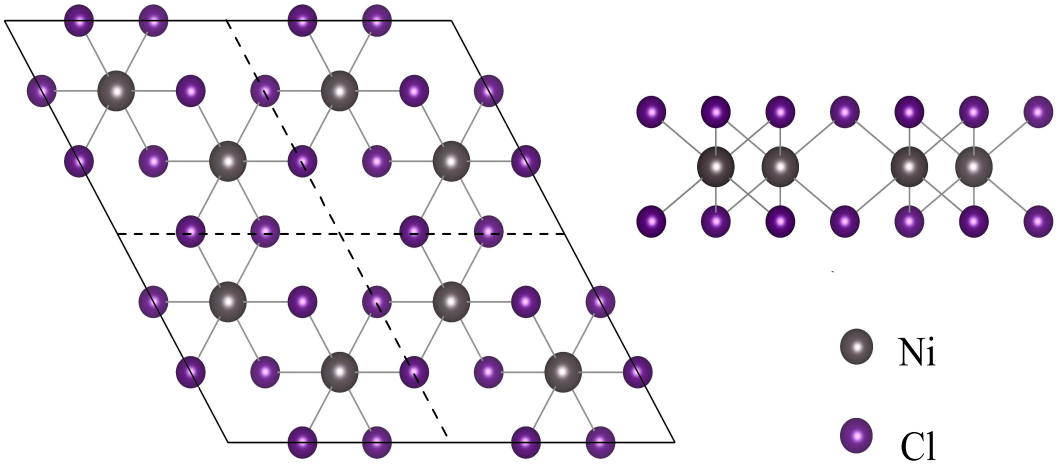

Figure 1. The top and side view of $NiCl_3$ monolayer, respectively.

The electronic properties of $NiCl_3$ monolayer are characterized by the electronic density of states (DOS) and electronic band structure, which are presented in Figure 2. Obviously, there is a bandgap of 1.17 eV and the Fermi level is in the gap for spin-down channel in the Figure 2a. The spin-up band is shown in Figure 2c. The valence and conduction band at Fermi level show linear energy dispersions with zero gap between conduction band minimum (CBM) and valence band maximum (VBM) at the high-symmetry K point, indicting Dirac spin-gapless states. Besides, the DOS in Figure 2b also shows that the spin-up state does not cross the Fermi level but has a zero band gap, while spin-down states has a 1.17 eV bandgap. Band edges of both spin channels consist of the *d*-orbital of the Ni atom and the *p*-orbital of the Cl atom, as shown by the projected DOS (PDOS) in the Figure 2d,e for Ni and Cl, respectively. As a result, $NiCl_3$ monolayer belongs to a Dirac spin-gapless semiconductor.

The effective mass (m^*_{ij}) in the vicinity of Fermi level, a crucial parameter for the transport behavior of semiconductor, can be extracted from using the existing band structure. Generally, m^*_{ij} can be obtained by $m^*_{ij} = \hbar^2 \left[\frac{\partial^2 E}{\partial k_i \partial k_j}\right]^{-1}$, where $\hbar$ is Plank's constant, i and j represent Cartesian coordinates. Based on the the VBM and CBM, the obtained values of m^* for the electron and hole carriers in both spin channels are listed in Table 1. By comparison, it can be found that the effective mass of the two carriers in the spin-up channel is much smaller than those in the spin-down channel, which is attributed to the linear energy dispersion in spin-up channel. In the spin-up channel, the effective mass of electrons (m^*_e = 0.28 m_e) is greater than that of holes (m^*_h = 0.23 m_e) due to the CBM is smoother than VBM, to which it is exactly opposite in the spin-down channel.

Table 1. The calculated effective mass (m^*), average effective mass (m_d), 2D elastic modulus (C_{2D}), DP constant (E_l), carrier mobility (μ), and relaxation time (τ) at the room temperature in both spin channels of $NiCl_3$ monolayer.

Spin Direction	Carrier Type	m^* (m_e)	m_d (m_e)	C_{2D} (N/m)	E_l (eV)	μ ($\times 10^3$ cm^2 V^{-1} s^{-1})	τ (fs)
Spin up	Electron	0.28	0.21	154.5	7.52	1.01	159.9
	Hole	0.23	0.18	154.5	7.52	1.39	182.7
Spin down	Electron	0.95	1.48	154.5	3.53	0.19	102.0
	Hole	6.10	8.29	154.5	7.76	0.001	3.8

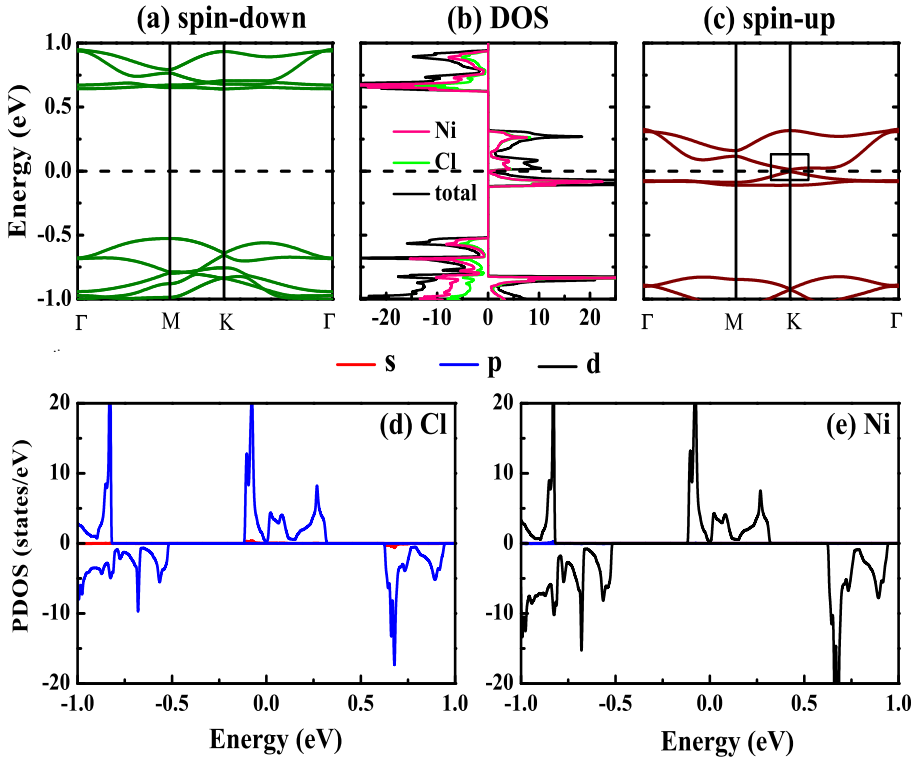

Figure 2. (**a**,**c**) are the calculated band structure for spin-down and spin-up channels of $NiCl_3$ monolayer, respectively. (**b**) is the total DOS and atom-resolved local DOS. (**d**,**e**) are the project DOS for the Ni and Cl atoms.

The carrier mobility (μ) is also a parameter to characterize the transport ability of carriers of $NiCl_3$ monolayer. Based on the Bardeen-Shockley deformation potential (DP) theory in two-dimensional materials, the carrier mobility in 2D lattice can be evaluated by [43–47]

$$\mu = \frac{e\hbar^3 C_{2D}}{k_B T m^* m_d E_l^2}, \tag{1}$$

where T is the thermodynamic temperature and k_B represents the Boltzmann constant. m_d denotes the average effective mass obtained by $m_d = \sqrt{m_x^* m_y^*}$ with m_x^* and m_y^* being effective mass along the x and y paths, respectively. E_l is the DP constant determined by

$$E_l = \frac{\partial E_{edge}}{\partial (l/l_0)}, \tag{2}$$

where E_{edge}, l and l_0 are the energy of CBM (or VBM), the deformation and equilibrium lattice constants, respectively. C_{2D} indicates the elastic constant of 2D structure in form of

$$C_{2D} = \frac{1}{S_0} \frac{\partial^2 E}{\partial (l/l_0)^2}, \tag{3}$$

where S_0 and E are the equilibrium cell area and the total energy for $NiCl_3$ monolayer. For the spin-up channel, since the CMB and VBM are in contact at point K, the values of E_{edge} at the CBM and VBM are exactly same, thus resulting an identical E_l of 7.52 eV. However, there are different E_l for holes (E_l = 7.76 eV) and electron (E_l = 3.53 eV) in the spin-down channel. The elastic modulus of $NiCl_3$ monolayer is 154.5 Nm^{-1}. Thus in the spin-up channel, the obtained mobilities of holes and electrons

are μ_h = 1.39 × 10^3 and μ_e = 1.01 × 10^3 cm^2 V^{-1} s^{-1}). The relaxation time τ of the carriers can then be estimated by $\tau = \mu m^*/e$. The resulting dependence of τ on T is shown in Figure 3. Obviously, τ decreases as the temperature increases and the degree of decline gradually decreases. All the needed parameters (m_d, E_l, C_{2d}, μ and τ) at room temperature are summarized in Table 1.

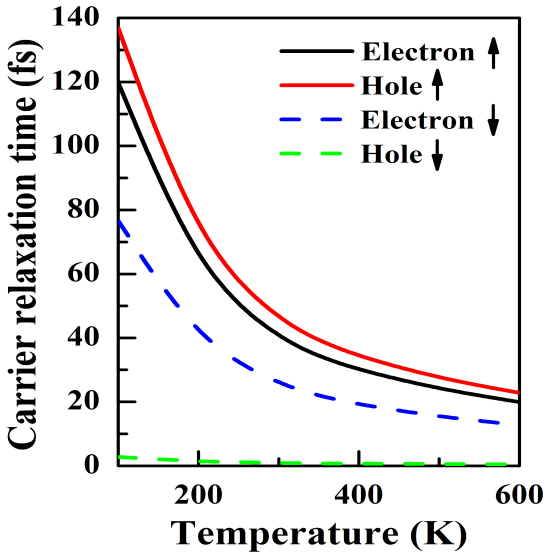

Figure 3. The obtained relaxation time for electron and hole for both spin channels when the temperature enhance from 100 K. ↑ (↓) represents spin-up (spin-down) direction.

3.2. Thermoelectric Properties

In order to explore the thermoelectric performance of $NiCl_3$ monolayer, we calculate thermoelectric transport parameters including S, σ and κ. Since the Curie temperature of $NiCl_3$ monolayer was predicted to be about 400 K by mean-field theory [10], we only take three typical temperatures (300, 350 and 400 K) in the whole calculations.

Firstly, we would like to examine the phonon transport properties of $NiCl_3$ monolayer, as the thermal transport in semiconductors is dominated by the phonons. The phonon spectra dispersions of $NiCl_3$ monolayer are shown in Figure 4a. Since each unit cell of $NiCl_3$ monolayer consists of eight atoms, its corresponding phonon dispersion has three acoustic phonon branches (ZA, TA and LA) and twenty-one optical phonon branches. The bottom three lines are acoustic phonon branches, and the others are optical branches branches. Due to the limited size of the supercell, the received phonon spectrum possesses minimal imaginary frequencies of 0.017 THz at the Γ point. Nevertheless, the structural stability of $NiCl_3$ monolayer is not affected by the size of supercell [10,52]. The dispersion of all the three acoustic modes is quite stronger away from the zone center, thus giving higher velocity modes than typical optical phonon and possess most of the heat. Moreover, there is no phonon gap between acoustic and optical branches, thus indicating a strong optical-acoustic phonon scattering which will suppress the κ_l. Figure 4b shows κ_l from 300 to 400 K. Obviously, the higher the temperature, the more intense the phonon scattering, so the κ_l decreases with increasing temperature. The value of κ_l at room temperature is 1.89 Wm^{-1} K^{-1} . Such a low κ_l implies that $NiCl_3$ monolayer could have favorable thermoelectric performance.

All samples have finite size in practical experiment and device application, thus the additional boundary scattering will reduce κ_l at nanoscale or at low temperatures. Here, the size effect is estimated from the κ_l as a function of the phonon mean free path (MFP). The computed κ_l as a function of phonon MFP at the temperature of 300, 350 and 400 K is shown in Figure 5. It can be seen that the range of phonon MFP that has significant effect on κ_l is approximately 10 to 150 nm. The characterized phonon MFP denoted by Λ can be obtained by fitting the acquired κ_l using a single parameter function [49]:

$$\kappa_l(\Lambda \leq \Lambda_{max}) = \frac{\kappa_{lmax}}{1 + \frac{\Lambda}{\Lambda_{max}}}, \quad (4)$$

where κ_{lmax} is κ of infinite size and Λ_{max} is maximal MFP. The Λ is 50.29, 41.79, and 36.97 nm at the temperature of 300 K, 350 K, and 400 K, respectively. This indicates that the κ_l of $NiCl_3$ monolayer may be drastically reduced when the sample size is several tens of nm. This feature is more conducive to the electronic and thermoelectric material based on $NiCl_3$ in low dimension.

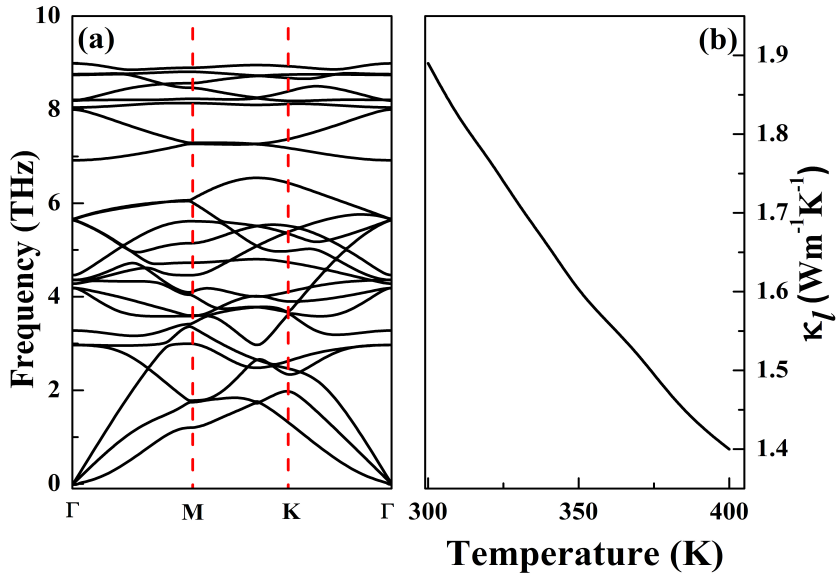

Figure 4. Phonon dispersion spectra (**a**) and lattice thermal conductivity (**b**) of $NiCl_3$ monolayer.

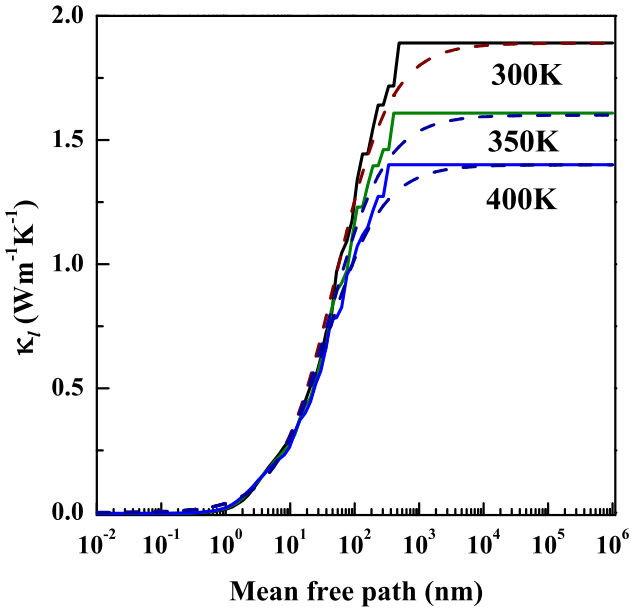

Figure 5. The obtained lattice thermal conductivities as a function of MFP at different temperatures. The fitted curves are indicated by dotted lines.

Secondly, the S, σ and κ_e can be evaluated based on the band structure. Figure 6a–d show the obtained Seebeck coefficient S in n- and p-type $NiCl_3$ monolayer as a function of carrier concentration (n) at T = 300, 350 and 400 K for the spin-up and spin-down channels, respectively. In the case of low carrier concentration, S is sensitive to temperature; the absolute value of S ($|S|$) is larger at low

temperatures such as 300 K. When the carrier concentration is above 1.0×10^{10} cm^{-2}, S is no longer dependent on temperature, but the $|S|$ decreases as the carrier concentration increases. The values of S for electrons and holes are almost identical in both spin channel. For example, at the carrier concentration of 1.15×10^{9} cm^{-2}, the $|S|$ is 1067 μVK^{-1} for the electron at the room temperature in the spin-up channel, which is comparable to 1048 μVK^{-1} for the hole. However, the $|S|$ in the spin-up channel is lower than the spin-down channel, although the spin-down channel exists a band gap. This indicates that the $|S|$ of $NiCl_3$ monolayer is determined by the band edge structure rather than the band gap.

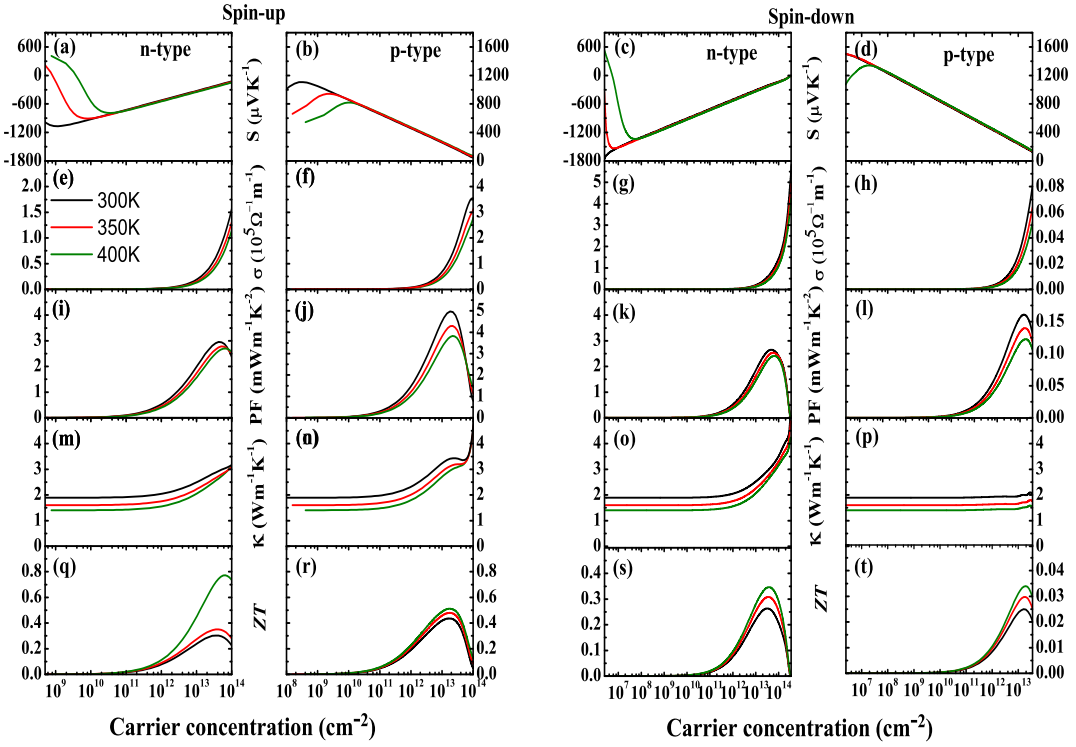

Figure 6. Seebeck coefficient S (**a**–**d**), electrical conductivity σ (**e**–**h**), power factor (PF) (**i**–**l**), total thermal conductivity (**m**–**p**) and zT value (**q**–**t**) of $NiCl_3$ monolayer for n-type and p-type in both directions as a function of the carrier concentration at the temperature of 300 K, 350 K, and 400 K.

The next four figures in Figure 6e–h show the dependence of electronic conductivity (σ) on carrier concentration at different temperatures. The σ increases significantly with increasing carrier concentration, but it is not sensitive to temperature. In the spin-up channel, the σ of the hole is larger than the electron under the same condition. Due to the relation $\sigma = ne\mu = ne2\tau/m_d^*$, the effective mass and relaxation time together determine the σ at a defined carrier concentration. P-type carriers possess smaller m^* and larger τ simultaneously, resulting in the greater mobility of carriers, so the σ is larger than that of n-type ones in this channel. In spin-down channel, the σ of the hole is lower than the electron, which can be explained by the data in Table 1. The two factors of PF ($S^2\sigma$), S and σ, show a opposite trend with increasing carrier concentration, which complicates the dependence of PF on carrier concentration. The calculated PF are presented in Figure 6i–l. It is obvious that the value of PF firstly increases to a maximum value and then slowly decreases with the further increases in carrier concentration. The maximal PF decreases slightly with increasing temperature. In particular, the PF of p-type is greater than that of the n-type carrier for the spin-up channel, because the n-type carrier has a larger σ and nearly similar S compared with the p-type one. This also predicts that the p-type $NiCl_3$ monolayer may has a higher zT value.

In order to obtain the final value of zT, we explored the total thermal conductivity (κ), which is shown in Figure 6m–p. The κ is mainly contributed by the κ_l, so it is not sensitive to the increase in

carrier concentration. The temperature has a large effect on κ, and increasing temperature leads to a decrease in κ. Based on the above discussions, we can estimated the zT value of $NiCl_3$ monolayer as a function of carrier concentration at three different temperatures (300, 350 and 400 K), which is exhibited in the last four figures in Figure 6q–t. In the spin-up channel, the maximal zT value is 0.3 (300 K), 0.35 (350 K), and 0.77 (400 K) for the *n*-type system, and the results are 0.44 (300 K), 0.48 (350 K), and 0.51 (400 K) for *p*-type one. Our calculations demonstrate that the $NiCl_3$ monolayer has a relatively high zT value and may be a promising thermoelectric material.

4. Conclusions

To summarize, we have investigated the thermoelectric performance as well as the structural and electronic properties of $NiCl_3$ monolayer by employing the *ab* initio calculations and semi-classical Boltzmann transport theory. Firstly, the the most stable crystal structure with a lattice constant of 5.96 Å and the dynamical stability are confirmed by the geometric optimization and phonon spectrum of $NiCl_3$ monolayer. Then the band structure indicates that $NiCl_3$ monolayer belongs to Dirac spin gapless semiconductor having almost massless carrier, high carrier mobility and fully spin-polarization. Based on the band structure of $NiCl_3$ monolayer, we estimate the effective mass, the carrier mobility and the relaxation time of the carriers by using deformation potential theory. Further, the thermoelectric parameters including seebeck coefficient, electric conductivity and electronic thermal conductivity are obtained by solving the phonon Boltzmann transport theory and the lattice thermal conductivity is evaluated by using phonon Boltzman transformation related to the harmonic and anharmonic interatomic force constants, and finally, the dimensionless figure of merit are evaluated according to the obtained thermoelectric parameters and the lattice thermal conductivity. As a result, $NiCl_3$ monolayer processes the optimum power factor of 4.97 mWm^{-1} K^{-2}, the lattice thermal conductivity of 1.89 Wm^{-1} K^{-1} and the dimensionless figure of merit of 0.44 at room temperature under reasonable carrier concentration. These features indicate that $NiCl_3$ monolayer may be a potential matrix for promising thermoelectrics.

Author Contributions: Conceptualization, J.L. and H.C.; methodology, X.C. and Y.H.; software, J.L. and Y.H. and X.C.; validation, H.Y.; formal analysis, J.L.; investigation, J.L.; resources, Y.H.; data curation, J.L.; writing–original draft preparation, J.L.; writing–review and editing, H.C.; visualization, J.L.; supervision, H.C.; project administration, H.C.; funding acquisition, H.C. All authors have read and agreed to the published version of the manuscript.

Funding: This research was funded by the National Natural Science Foundation of China under grant numbers 11875226 and 11874306, and the Natural Science Foundation of Chongqing under grant Number CSTC-2017jcyjBX0035.

Conflicts of Interest: The authors declare no conflict of interest.

References

1. McGuire, M.A. Crystal and magnetic structures in layered, transition metal dihalides and trihalides. *Crystals* **2017**, *7*, 121. [CrossRef]
2. Huang, B.; Clark, G.; Moratalla, E.N.; Klein, D.R.; Cheng, R.; Seyler, K.L.; Zhong, D.; Schmidgall, E.; McGuire, M.A.; Cobden, D.H.; et al. Layer-dependent ferromagnetism in a van der Waals crystal down to the monolayer limit. *Nature* **2017**, *546*, 270–273. [CrossRef] [PubMed]
3. McGuire, M.A.; Yan, J.Q.; Kelley, P.L.; May, A.F.; Cooper, V.R.; Lindsay, L.; Puretzky, A.; Liang, L.B.; Santosh, K.C.; Cakmak, E.; et al. High-temperature magnetostructural transition in van der Waals-layered α-$MoCl_3$. *Phys. Rev. Mater.* **2017**, *1*, 064001. [CrossRef]
4. Seyler, K.L.; Zhong, D.; Klein, D.R.; Gao, S.Y.; Zhang, X.O.; Huang, B.; Moratalla, E.N.; Yang, L.; Cobden, D.H.; McGuire, M.A.; et al. Ligand-field helical luminescence in a 2D ferromagnetic insulator. *Nat. Phys.* **2018**, *14*, 277–281. [CrossRef]
5. Zhang, W.B.; Qu, Q.; Zhu, P.; Lam, C.H. Robust intrinsic ferromagnetism and half semiconductivity in stable two-dimensional single-layer chromium trihalides. *J. Mater. Chem. C* **2015**, *3*, 12457–12468. [CrossRef]
6. Liu, J.Y.; Sun, Q.; Kawazoe, Y.; Jena, P. Exfoliating biocompatible ferromagnetic Cr-trihalide monolayers. *Phys. Chem. Chem. Phys.* **2016**, *18*, 8777–8784. [CrossRef]

7. Zhou, Y.G.; Lu, H.F.; Zu, X.T.; Gao, F. Evidencing the existence of exciting half-metallicity in two-dimensional $TiCl_3$ and VCl_3 sheets. *Sci. Rep.* **2016**, *6*, 19407. [CrossRef]
8. He, J.J.; Ma, S.Y.; Lyu, P.B.; Nachtigall, P. Unusual Dirac half-metallicity with intrinsic ferromagnetism in vanadium trihalide monolayers. *J. Mater. Chem. C* **2016**, *4*, 2518–2526. [CrossRef]
9. Weber, D.; Schoop, L.M.; Duppel, V.; Lippmann, J.M.; Nuss, J.; Lotsch, B.V. Magnetic properties of restacked 2D spin 1/2 honeycomb $RuCl_3$ nanosheets. *Nano Lett.* **2016**, *16*, 3578–3584. [CrossRef]
10. He, J.J.; Li, X.; Lyu, P.B.; Nachtigall, P. Near-room-temperature Chern insulator and Dirac spin-gapless semiconductor: Nickel chloride monolayer. *Nanoscale* **2017**, *9*, 2246–2252. [CrossRef]
11. Sheng, X.L.; Nikolic, B.K. Monolayer of the 5d transition metal trichloride $OsCl_3$: A playground for two-dimensional magnetism, room-temperature quantum anomalous Hall effect, and topological phase transitions. *Phys. Rev. B* **2017**, *95*, 201402. [CrossRef]
12. Sarikurt, S.; Kadioglu, Y.; Ersan, F.; Vatansever, E.; Akturk, O.; Yuksel, Y.; Akinci, U.; Akturk, E. Electronic and magnetic properties of monolayer $RuCl_3$: A first-principles and Monte Carlo study. *Phys. Chem. Chem. Phys.* **2018**, *20*, 997–1004. [CrossRef] [PubMed]
13. Iyikanat, F.; Yagmurcukardes, M.; Senger, R.; Sahin, H. Tuning electronic and magnetic properties of monolayer α-$RuCl_3$ by in-plane strain. *J. Mater. Chem. C* **2018**, *6*, 2019–2025. [CrossRef]
14. Sun, Q.L.; Kioussis, N. Prediction of manganese trihalides as two-dimensional Dirac half-metals. *Phys. Rev. B* **2018**, *97*, 094408. [CrossRef]
15. Ersan, F.; Vatansever, E.; Sarikurt, S.; Yuksel, Y.; Kadioglu, Y.; Ozaydin, H.D.; Akturk, O.U.; Akinci, U.; Akturk, E. Exploring the electronic and magnetic properties of new metal halides from bulk to two-dimensional monolayer: RuX_3 (X=Br, I). *J. Magn. Magn. Mater.* **2019**, *476*, 111–119. [CrossRef]
16. Tomar, S.; Ghosh, B.; Mardanya, S.; Rastogi, P.; Bhadoria, B.S.; Chauhan, Y.S.; Agarwal, A.; Bhowmick, S. Intrinsic magnetism in monolayer transition metal trihalides: A comparative study. *J. Magn. Magn. Mater.* **2019**, *489*, 165384. [CrossRef]
17. Zhang, W.X.; Li, Y.; Jin, H.; She, Y.C. Two-dimensional transition-metal halide $CoBr_3$ with spin-polarized Dirac cone. *Phys. Chem. Chem. Phys.* **2019**, *21*, 17740. [CrossRef]
18. Wang, X.T.; Li, T.Z.; Cheng, Z.X.; Wang, X.L.; Chen, H. Recent advances in Dirac spin-gapless semiconductors. *Appl. Phys. Rev.* **2018**, *5*, 041103. [CrossRef]
19. Mahan, G.D.; Sofo, J.O. The best thermoelectric. *Proc. Natl. Acad. Sci. USA* **1996**, *93*, 7436–7439. [CrossRef]
20. DiSalvo, F.J. Thermoelectric cooling and power generation. *Science* **1999**, *285*, 703–706. [CrossRef]
21. Snyder, G.J.; Toberer, E.S. Complex thermoelectric materials. *Nat. Mater.* **2008**, *7*, 105–114. [CrossRef]
22. Hicks, L.D.; Dresselhaus, M.S. Effect of quantum-well structures on the thermoelectric figure of merit. *Phys. Rev. B* **1993**, *47*, 12727–12731. [CrossRef] [PubMed]
23. Hicks, L.D.; Dresselhaus, M.S. Thermoelectric figure of merit of a one-dimensional conductor. *Phys. Rev. B* **1993**, *47*, 16631–16634. [CrossRef] [PubMed]
24. Dresselhaus, M.S.; Chen, G.; Tang, M.Y.; Yang, R.G.; Lee, H.; Wang, D.Z.; Ren, Z.F.; Fleurial, J.P.; Gogna, P. New directions for low-dimensional thermoelectric materials. *Adv. Mater.* **2007**, *19*, 1043–1053. [CrossRef]
25. Hung, N.T.; Hasdeo, E.H.; Nugraha, A.R.T.; Dresselhaus, M.S.; Saito, R. Quantum Effects in the Thermoelectric Power Factor of Low-Dimensional Semiconductors. *Phys. Rev. Lett.* **2016**, *117*, 036602. [CrossRef]
26. Chen, X.R.; Huang, Y.H.; Liu, J.; Yuan, H.K.; Chen, H. Thermoelectric performance of two-dimensional AlX (X = S, Se, Te): A first-principles-based transport study. *ACS Omega* **2019**, *4*, 17773–17781. [CrossRef]
27. Kresse, G.; Hafner, J. Ab initio molecular dynamics for liquid metals. *Phys. Rev. B* **1993**, *47*, 558–561. [CrossRef]
28. Kresse, G.; Hafner, J. Ab initio molecular-dynamics simulation of the liquid-metal-amorphous-semiconductor transition in germanium. *Phys. Rev. B* **1994**, *49*, 14251–14269. [CrossRef]
29. Kresse, G.; Furthmuller, J. Efficiency of ab-initio total energy calculations for metals and semiconductors using a plane-wave basis set. *Comput. Mater. Sci.* **1996**, *6*, 15–50. [CrossRef]
30. Blochl, P.E. Projector augmented-wave method. *Phys. Rev. B* **1994**, *50*, 17953–17979. [CrossRef]
31. Perdew, J.P.; Burke, K.; Ernzerhof, M. Generalized gradient approximation made simple. *Phys. Rev. Lett.* **1996**, *77*, 3865–3868. [CrossRef] [PubMed]
32. Monkhorst, H.J.; Pack, J. Special points for Brillouin-zone integrations. *Phys. Rev. B* **1976**, *13*, 5188–5192. [CrossRef]

33. Madsen, G.K.H.; Singh, D.J. BoltzTraP. A code for calculating band-structure dependent quantities. *Comput. Phys. Commun.* **2006**, *175*, 67–71. [CrossRef]
34. Bilc, D.I.; Hautier, G.; Waroquiers, D.; Rignanese, G.M.; Ghosez, P. Low-Dimensional transport and large thermoelectric power factors in bulk semiconductors by band engineering of highly directional electronic states. *Phys. Rev. Lett.* **2015**, *114*, 136601. [CrossRef]
35. He, J.; Amsler, M.; Xia, Y.; Naghavi, S.; Hegde, V.; Hao, S.; Goedecker, S.; Ozolins, V.; Wolverton, C. Ultralow thermal conductivity in full Heusler semiconductors. *Phys. Rev. Lett.* **2016**, *117*, 046602. [CrossRef]
36. Wickramaratne, D.; Zahid, F.; Lake, R.K. Electronic and thermoelectric properties of van der Waals materials with ring-shaped valence bands. *J. Appl. Phys.* **2015**, *118*, 075101. [CrossRef]
37. Cai, Y.Q.; Zhang, G.; Zhang, Y.W. Polarity-reversed robust carrier mobility in monolayer MoS_2 nanoribbons. *J. Am. Chem. Soc.* **2014**, *136*, 6269–6275. [CrossRef]
38. Long, M.Q.; Tang, L.; Wang, D.; Wang, L.J.; Shuai, Z.G. Theoretical predictions of size-dependent carrier mobility and polarity in graphene. *J. Am. Chem. Soc.* **2009**, *131*, 17728–17729. [CrossRef]
39. Hung, N.T.; Nugraha, A.R.T.; Saito, R. Two-dimensional InSe as a potential thermoelectric material. *Appl. Phys. Lett.* **2017**, *111*, 092107. [CrossRef]
40. Jiang, P.H.; Liu, H.J.; Cheng, L.; Fan, D.D.; Zhang, J.; Wei, J.; Liang, J.H.; Shi, J. Thermoelectric properties of gamma-graphyne from first-principles calculations. *Carbon* **2017**, *113*, 108–113. [CrossRef]
41. Liao, B.; Zhou, J.; Qiu, B.; Dresselhaus, M.S.; Chen, G. Ab initio study of electron-phonon interaction in phosphorene. *Phys. Rev. B* **2015**, *91*, 235419. [CrossRef]
42. Bardeen, J.; Shockley, W. Deformation potentials and mobilities in non-polar crystals. *Phys. Rev.* **1950**, *80*, 72–80. [CrossRef]
43. Fei, R.X.; Faghaninia, A.; Soklaski, R.; Yan, J.A.; Lo, C.; Yang, L. Enhanced thermoelectric efficiency via orthogonal electrical and thermal conductances in phosphorene. *Nano Lett.* **2014**, *14*, 6393–6399. [CrossRef] [PubMed]
44. Dai, J.; Zeng, X.C. Titanium trisulfide monolayer: Theoretical prediction of a new direct-gap semiconductor with high and anisotropic carrier mobility. *Angew. Chem.* **2015**, *54*, 7572–7576. [CrossRef]
45. Wang, J.; Xie, F.; Cao, X.H.; An, S.C.; Zhou, W.X.; Tang, L.M.; Chen, K.Q. Excellent thermoelectric properties in monolayer WSe_2 nanoribbons due to ultralow phonon thermal conductivity. *Sci. Rep.* **2017**, *7*, 41418. [CrossRef] [PubMed]
46. Zhang, J.; Liu, X.; Wen, Y.; Shi, L.; Chen, R.; Liu, H.; Shan, B. Titanium trisulfide monolayer as a potential thermoelectric material: A first-principles-Based Boltzmann transport study. *ACS Appl. Mater.* **2017**, *9*, 2509–2515. [CrossRef]
47. Wang, F.Q.; Guo, Y.; Wang, Q.; Kawazoe, Y.; Jena, P. Exceptional thermoelectric properties of layered $GeAs_2$. *Chem. Mater.* **2017**, *29*, 9300–9307. [CrossRef]
48. Li, W.; Carrete, J.; Katcho, N.; Mingo, N. ShengBTE: A solver of the Boltzmann transport equation for phonons. *Comput. Phys. Commun.* **2014**, *185*, 1747–1758. [CrossRef]
49. Li, W.; Lindsay, L.; Broido, D.; Stewart, D.; Mingo, N. Thermal conductivity of bulk and nanowire $Mg_2Si_xSn_{1-x}$ alloys from first principles. *Phys. Rev. B* **2012**, *86*, 174307. [CrossRef]
50. Li, W.; Mingo, N.; Lindsay, L.; Broido, D.; Stewart, D.; Katcho, N. Thermal conductivity of diamond nanowires from first principles. *Phys. Rev. B* **2012**, *85*, 195436. [CrossRef]
51. Togo, A.; Oba, F.; Tanaka, I. First-principles calculations of the ferroelastic transition between rutile-type and $CaCl_2$-type SiO_2 at high pressures. *Phys. Rev. B* **2008**, *78*, 134106. [CrossRef]
52. Sahin, H.; Cahangirov, S.; Topsakal, M.; Bekaroglu, E.; Akturk, E.; Senger, R.T.; Ciraci, S. Monolayer honeycomb structures of group-IV elements and III-V binary compounds: First-principles calculations. *Phys. Rev. B* **2009**, *80*, 155453. [CrossRef]